A comparison of state-of-the-art image evaluation techniques for analysis of opaque flows

Karsten Staack*[1], Steve Wereley[2], Christoph S. Garbe[1], Christian Willert[3]

1: Interdisciplinary Center for Scientific Computing, University of Heidelberg, Germany
2: School of Mechanical Engineering, Purdue University, West Lafayette, IN 47907, USA
3: Institute of Propulsion Technology, German Aerospace Center (DLR), 51170 Köln, Germany
*correspondent author: karsten.staack@iwr.uni-heidelberg.de

Abstract In this paper we compare state-of-the-art fluid motion estimation algorithms with respect to the application to opaque flow images, such as *Particle Image Velocimetry* (PIV), *Optical Flow* and specialized variants of these. In order to compare the outcome of the algorithms we perform turbulent jet experiments with different Reynolds numbers to generate opaque images with a known average flow field as a reference to estimate the errors. Thereafter the algorithms are used to estimate the velocity of a submerged oil/gas plume that was recorded by an observation camera. We will show that the estimates strongly depend on the choice of algorithm, especially for field test images where cloud-like image structures are the only information to retrieve the motion.

1. Introduction

Todays image motion algorithms in fluid dynamics are highly developed and accurate down to velocities of fractions of a pixel per frame. This is due to the fact that the algorithms are extremely tuned to deal with a certain type of images that are provided by fluid experimentalists. Especially *Particle Image Velocimetry* (PIV) and the corresponding images (Okamoto et al, 2000) are strongly coupled in a way that the algorithm produces less accurate results when it is applied to "non-ideal" images like opaque images with large and mostly smooth intensity structures. In field test situation it is usually not possible to set up the visualization in such a way that it suits the motion estimation algorithm. Examples are satellite images of cloud motion (Corpetti et al, 2002) or the motion of people around obstacles (Corpetti and Courty, 2007). But also in many laboratory or field measurement setups it is sometimes hard to visualize the flow in order to be properly processed by motion estimators. Since mostly particles are used to render the flow visible, investigators run into troubles if the measurement section is too large because the particle size is fixed (Bosbach et al, 2009). On the other hand, if the area of interest is too small (micro fluidic), the particles might interfere with the flow characteristics and other tracers have to be used Garbe et al (2008).

The deficiency of not knowing which motion algorithm performs best on what images became evident after the oil rig accident in the Gulf of Mexico in April 2010 which led to the loss of the Deepwater Horizon rig and severed the drill pipe at the sea floor. In the weeks following the incident streaming video sequences of the failure site was provided by subsea remotely operated vehicles (ROV) and subsequently analyzed by numerous investigators in an effort to estimate oil release rates. It turned out that this is by far a more difficult task then previously expected since standard motion estimation techniques have difficulties to yield trustworthy results. Several researchers came up with estimates, that differ extremely and also had large confidence intervals (Flow Rate Technical Group, 2010; Crone, 2010). The aim of the present work is to compare the most prominent motion algorithms with respect to their accuracy and deficiencies on fluid motion images similar to the oil spill images.

In order to be able quantitatively compare the motion algorithms a reference data set with known flow properties is required. Plenty of such data sets exist visualizing the motion with particles but very few with image structures resembling those of the oil/gas mixture issuing from the failed oil rig

site (Figure 1). Measurements by Crone et al (2008) and Savaş (2011) provide comparable images but do not match our requirements in terms of spatial resolution, temporal resolution and existence of distinctly traceable flow structures. Therefore a laboratory experiment satisfying these conditions was conducted to provide long image sequences of a known flow field. The experimental setup and execution is described in the following section. The image sequences are then processed by an assortment of motion algorithms that are briefly explained in the section 3. Since the flow characteristics of the experiment are known, the accuracy of the respective algorithms can be estimated. To demonstrate the suitability of these algorithms for flow estimation in a real-world situation the second part of this paper presents results obtained by processing an image sequence of a subsea oil/gas plume provided by an ROV.

Tab. 1. Sample image from the ROV observation video picturing the failure site with the oil spill

configuration		**1**	**2**	**3**
volume flow j	$[^{\mathrm{l}}/_{\mathrm{h}}]$	250	300	400
exit velocity U_0	$[^{\mathrm{m}}/_{\mathrm{s}}]$	1.28	1.54	2.05
Reynolds number Re	$[-]$	10610	12733	16977
max. displacement $d_{\max}$	$[\mathrm{mm}]$	0.64	0.77	1.027
max. displacement $d_{\max}$	$[\mathrm{px}]$	6.50	7.79	10.39

Tab. 2. Configuration table of the measurements

2. Opaque flow image sequences

2.1 Previous experiments

Given that dye visualization sequences are difficult to process in comparison to particle based visualizations (e.g. PIV, particle tracking), little effort has been invested in the past in producing adequate experimental images. To the knowledge of the authors there are only a few investigations dealing with opaque plume or jet flows. Noteworthy is the work by Crone Crone et al (2008) who attempted to estimate the outflow of black smokers which are hydrothermal vents found on the ocean seabed. For this purpose he acquired image sequences of a buoyant jet experiment at Reynolds numbers ($2,900 \leq \mathrm{Re} \leq 6,700$). The visualization was done by graphite particles that were illuminated by halogen lamps.

More recently, researchers paid attention to the task of estimating the volume outflow of the Deepwater Horizon failure site. Crone applied his estimation technique to video sequences provided by the ROVs (Crone et al, 2008). As part of the Deepwater Horizon incident investigation the Flow Rate Technical Group (FRTG) was formed and assigned with the task of surveying numerous approaches in assessing the oil discharge rates from the failure site (McNutt et al, 2011). In this context Savaş performed several jet experiments that used dye to visualize the jet ($32,000 \leq \mathrm{Re} \leq 223,000$) (Savaş, 2011). The dye was injected into the jet fluid and mixed homogeneously prior to discharge from the jet nozzle. This led to the absence of distinctly visible dye structures within the flow as it exits the nozzle. On the other hand it is sharply bounded towards the transparent fluid surrounding the jet. This homogeneity limited the velocity estimation to tracking of the interface. Dye features in the jet were tracked manually.

None of these two experimental data sets match the requirements of the present investigation because on the one side Crone's data is of limited spatial resolution while Savaş' data does not allow

a dense velocity field estimation across the entire jet. Consequently, for our algorithmic comparison we conducted specific laboratory experiments to produce adequate image sequences.

2.2 Laboratory experiment

A water jet was introduced vertically into a water basin using a nozzle of 8.3 mm diameter (Fig. 1). The transparent acrylic glass water tank was sufficiently large ($1.3\,m \times 0.7\,m \times 0.2\,m$) to maintain an undisturbed jet profile up to a downstream distance of $30\,D$. The flow was visualized by injection of a blue dye solution (Patent Blue V, 1.5 g/l) near the nozzle. This way the dye was not entirely mixed prior to discharge from the nozzle which results in traceable dye structures throughout the entire jet (Fig. 2). Three jet configurations were measured (see table 2).

Since the jet is highly turbulent with the flow structures evolving quite rapidly, images were acquired with a high speed camera (*PCO GmbH, DIMAX Color*) at a frame rate of 2000 Hz and a spatial resolution of 2016×1092 pixels. The lens was a Nikkor 90 mm which provided a sufficiently large field of view. Another benefit of this camera is its high sensitivity and large dynamic range of 12 bits per color channel. Six halogen lamps and an optical diffuser were used to produce a uniform background illumination. The lamps were operated with a constant current power source to avoid intensity variations through 50 Hz AC line power.

A momentum diffuser was positioned in the lower part of the basin to enforce dissipation of turbulent structures and prevent the onset of recirculation within the tank. The jet was operated in a continuous fashion while the dye was added just prior to each measurement. The size of the water tank was sufficient to measure 1 min before the dye circulated back to the nozzle. To achieve convergence of higher order statistics the the camera was set to acquire a maximum number of images (11642) at the selected resolution which corresponds to about 5.8 sec.

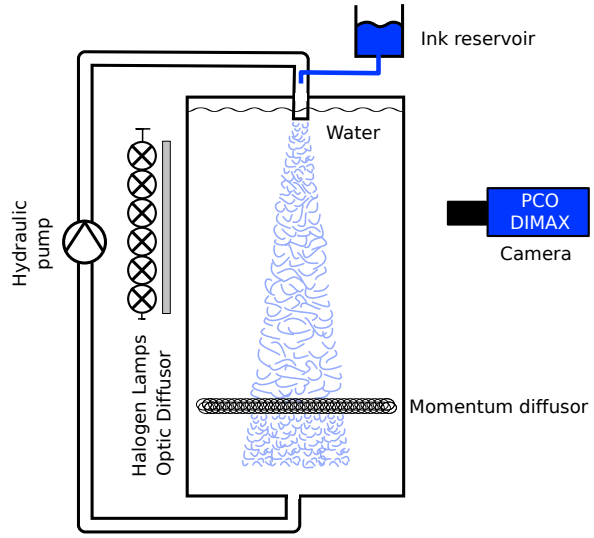

Fig. 1. Scheme of the laboratory experiment

Fig. 2. Image example from the recorded data

3. Methods

Prior to the brief description of the algorithms, we give account of our notation to avoid misconceptions and to simplify the equations. In the following, $\Omega := \{(x_i, y_i) \mid i = 1 \dots M\}$ denotes the discrete spatial domain of the image, which means it is the set that includes all M pixel positions of the image. The images are functions defined on Ω and the discrete temporal domain $\mathcal{T} := \{t_j \mid j = 1 \dots N\}$ that map onto the real numbers $\mathbb{R}$. For better readability we omit the temporal variable t_i in the arguments and indicate the time dependency by an index $I_i(x, y) := I(x, y, t_i)$. Using this notation, all algorithms can be written rather simple. Since the aim is to determine the average flow field $\bar{u}$, we present

algorithms that include the entire image sequence for the estimation. Since the velocity field $\bar{u}$ equals the displacement field $\bar{d}$ up to the constant Δt, we use $\bar{d}$ as the desired solution in the algorithms to avoid unnecessary confusion caused by additional variables.

3.1 Minimum Quadratic Difference (MQD)

The fundamental assumption of basic motion estimation on images is that pixel intensity changes are only caused by their motion. Thus the image intensity can be considered a conserved quantity which means that the accumulated pixel intensity over any two images I_i, I_j of the sequence is constant: $\sum_\Omega I_i = \sum_\Omega I_j$. Therefore, the displacement field $d(x)$ can be recovered by reversing the distortion of the motion in the first place. We need a mathematical norm to quantify the degree of matching between two images. Common metrics are the *mean squared error* (MSE) or the *sum of squared errors* (SSE) that are frequently used in regression analysis. Due to noise and a simplistic dynamical model, we can not expect to match both images perfectly by distorting one of them. Hence, we try to find the displacement field $d(x)$ that minimizes the SSE.

$$\bar{d}^{MQD}(x) = \frac{1}{N-1} \sum_{i=1}^{N-1} \arg\min_{d_i} \sum_\Omega \omega(x) \left[I_i(x) - I_{i+1}(x - d_i) \right]^2 \tag{1}$$

This approach was introduced by Gui and Merzkirch (1996) for particle images in fluid dynamics, but was named *minimum quadratic differences* (MQD). This parameter estimation problem cannot be solved for each pixel since there are two unknowns (u, v) and only one equation (1) per pixel. The problem can be solved uniquely by imposing a second constraint. Often, the assumption of identical inherent motion in a local neighborhood is such a constraint that allows to pool the motion constraint. This leads to an overdetermined system of equations. Practically, *one* motion estimate for a small neighborhood around x is estimated. The neighborhood is defined by a windowing function ω. In the simplest case ω is a boxcar function centered around x. More general it can be any positive function with $\sum_\Omega \omega(x) = 1$ (Astarita, 2007).
We want to point out, that this approach is the starting point of other motion estimation algorithms. Cross correlation techniques can be derived by expanding the brackets and neglecting some terms. Optical flow can be derived by performing a Taylor approximation around small displacements $d(x)$. The benefits of these other techniques are mainly for practical reasons, since they lead to efficient algorithms to find the sought solution.

3.2 Cross correlation (CC)

The most commonly used algorithm in experimental fluid dynamics is based on cross correlation of image patches. The foremost technique is *Particle Image Velocimetry* (PIV) (Raffel et al, 2007). It is meant to deal with flows that are visualized by small particles whose motion can be used to deduce the motion of the fluid flow. A unique matching of individual particles between frames is not possible. Equivalent to MQD the average displacement field $\bar{d}$ can be approximated by estimating the mean velocity of a small local neighborhood using the weighting function ω which contains multiple particles (Willert and Gharib, 1991). However, this corresponds to a spatial averaging and thus decreases the spatial resolution. The displacement $d(x)$ is found by searching for the best correlation with respect to a certain shift of one image patch against the other. Fitting methods help to achieve spatial resolutions up to fractions of a pixel.
There are several approaches to estimate an average velocity field (Meinhart et al, 2000). The most common approach is to estimate the instantaneous motion from two consecutive images and to aver-

age the velocity fields subsequently. This method can be formulated as follows:

$$\bar{d}^{CC} = \frac{1}{N-1} \sum_{i=1}^{N-1} \arg\max_{d_i} \frac{\sum_\Omega \omega(x) I_i(x) I_{i+1}(x-d_i)}{\sqrt{\sum_\Omega \omega(x) I_i^2(x) \sum_\Omega \omega(x) I_{i+1}^2(x-d_i)}} \tag{2}$$

It should be noted that for correlation based techniques, most often the Fourier transform is used to reduce the computational effort. Another benefit is that the patches in both images can be equally large. This transform is accompanied by a periodic repetition of the image itself beyond the borders. As a consequence, both factors in the denominator are independent of d_i and are therefore constants which can be easily calculated. A way to circumvent the induced errors is to perform direct correlations (McKenna and McGillis, 2002) or use multiple Fourier transforms (Ronneberger et al, 1998). This becomes especially apparent for small neighborhoods ($|\operatorname{supp}(w)|$ is small).
However, Meinhart et al (2000) showed that amongst the three averaging method they investigated, vector field averaging is inferior with respect to accuracy and robustness. The next method describes the averaging, that performed best according to them.

3.3 Cross correlation averaging (CCA) and Ensemble Minimum Quadratic Difference (EMQD)

An alternative method to estimate the average velocity is *cross correlation averaging* (CCA) (Meinhart et al, 2000) which averages the individual correlations before detecting the displacement as indicated in equation 3. Merely the minimization and the summation over the images are switched, which makes a big difference, since $\arg\max$ is nonlinear. The advantage over the previous method in equation 2 is that no information is discarded before the maximization. This way it is more robust against erroneous estimates since entire correlation are averaged rather than just the positions of the maximum.

$$\bar{d}^{CCA} = \arg\max_{d} \sum_{i=1}^{N-1} \frac{\sum_\Omega \omega(x) I_i(x) I_{i+1}(x-d)}{\sqrt{\sum_\Omega \omega(x) I_i^2(x) \sum_\Omega \omega(x) I_{i+1}^2(x-d)}} \tag{3}$$

Instead of determining multiple displacement fields, this algorithm provides a single result which is the best match to the entire sequence. In the same manner MQD can be transferred to an ensemble averaging method (EMQD).

$$\bar{d}^{EMQD}(x) = \arg\min_{d} \sum_{i=1}^{N-1} \sum_{\Omega} \omega(x) \left[I_i(x) - I_{i+1}(x-d) \right]^2 \tag{4}$$

3.4 Pixel matching (PM)

This method is basically a two-point spatio-temporal correlation. In contrast to the two previous methods, the averaging is not done in the spatial dimension but in the temporal dimension. The advantage is that there is no loss of spatial resolution. Even though there might be no particle (or distinct image feature) at all locations in the individual images at all time steps, the temporal averaging can make up for this because once in a while particles will pass by.

$$\bar{d}^{PM} = \arg\max_{d} \frac{\sum_{i=1}^{N-1} \hat{I}_i(x) \hat{I}_{i+1}(x-d)}{\sqrt{\sum_{i=1}^{N-1} \hat{I}_i^2(x) \sum_{i=1}^{N-1} \hat{I}_{i+1}^2(x-d)}} \tag{5}$$

In order to simplify the equation we introduced $\hat{I}_i(x) := I_i(x) - \sum_{i=1}^{N-1} I_i(x)$ which is the temporal intensity fluctuation of the pixel at location x. For correctness we have to mention, that the summation for $\hat{I}_{i+1}(x)$ starts at $i = 2$ and ends at N. This way we deal with a normalized cross correlation and

a value range between $[-1, 1]$. This approach was proposed by Delnoij et al (1999) and later referred to as *single pixel ensemble correlation* by Westerweel et al (2004). The advantage of having a dense motion estimation comes with the drawback of storing spatio-temporal dependencies for each pixel with a set of neighboring pixels and also a slow brute-force algorithm to calculate it.

3.5 Time-Matching (TM)

This algorithm is the equivalent to pixel matching (PM) but in the temporal domain. The time series of two pixels are cross correlated to obtain the average time lag δt. By setting the distance of two pixels δx a priori and knowing the separation time Δt between the image frames it is possible to determine the average velocity.

$$\bar{d}^{TM} = \delta x \Delta t \left[\arg\max_{\delta t} \sum_{i=1}^{N-1} I(x,t) I(x+\delta x, t+\delta t) dt \right]^{-1} \tag{6}$$

This method is analogue to multiple hot-wire measurements, where the temporal signals are correlated in order to determine the dependency.

3.6 Optical Flow (OF)

Optical flow is probably the most prominent gradient based method for motion estimation (Barron et al, 1994)(Beauchemin and Barron, 1995). It originates from computer vision applications where for instance the motion of cars or persons has to be estimated from surveillance sequences. More recently it has found application in fluid dynamics (Quénot et al, 1998)(Corpetti et al, 2002)(Corpetti et al, 2005). The most prominent optical flow algorithm was proposed by Horn and Schunck (1981). Optical flow can be derived from the MQD cost functional by Taylor approximation which leads to a differential conservation equation of the pixel intensity (*brightness constancy constraint*).

$$\bar{d}^{OF} = \frac{\Delta t}{N-1} \sum_{i=1}^{N-1} \arg\min_{u_i} \left\{ \sum_{\Omega} \left[u_i^T \nabla I_i + \partial_t I_i \right]^2 + \frac{\alpha}{2} \sum_{\Omega} \left[\nabla u_i \right]^2 \right\} \tag{7}$$

In order to render the problem solvable, Horn and Schunck (1981) added a regularizing term, which controls the smoothness of the solution. The parameter α balances between the data and regularizing term. Consequently, large motion variations between neighboring pixels are penalized which is reasonable for most fluid dynamics applications.

3.7 Ensemble Optical Flow (EOF)

Similar to cross correlation and cross correlation averaging it is possible to merge the temporal averaging into the solution finding process. Instead of estimating many instantaneous velocity fields via optical flow, the task is to find *one* velocity field that is the best fit to the entire image sequence. This concept was already proposed by Staack and Garbe (2011) and is similar to the optical flow algorithm by Lucas and Kanade (1981) with the difference that the temporal averaging does not reduce the spatial resolution. It is very efficient to evaluate since only pairwise correlations of image gradients $(\nabla I, \partial_t I)$ have to be calculated. Also, the algorithm allows parallelization since each pixel can be treated independently (for $\alpha = 0$).

$$\bar{d}^{EOF} = \arg\min_{u} \left\{ \sum_{\Omega} \sum_{i=1}^{N-1} \left[u^T \nabla I_i + \partial_t I_i \right]^2 + \frac{\alpha}{2} \sum_{\Omega} \left[\nabla u \right]^2 \right\} \tag{8}$$

Comparable to Lucas and Kanade (1981), validation measures exist that mainly originate from matrix analysis. They make it feasible to extract the quality of motion information in each pixel. This is a benefit over optical flow which lacks a reliable confidence indicator.

4. Results of jet flow

The main challenge of analyzing opaque flows is that the actual centerline velocity of the jet is occluded by vortical structures that appear randomly. The velocity of all visualized structures are integrated over a pixel's line of sight. As a consequence, average velocity algorithms as proposed above, are not an adequate choice to determine the centerline velocity. In any case, the velocity will be underestimated since the average optical penetration depth into the opaque jet is not the centerline but somewhere off-axis. However, if the optical penetration depth would be known exactly, one could connect this information through an optimization approach to theoretical jet models in order to estimate the centerline velocity. The most accurate estimate we achieve is where hardly any vortical structures (Kelvin-Helmholtz instabilities) appear. The region close to the nozzle suits this requirement best. Therefore, we expect the algorithms to achieve their best estimate in the near-field of the jet. This is precisely what becomes apparent throughout the results of all motion estimators.

4.1 Minimum Quadratic Difference and Ensemble Minimum Quadratic Difference

The two figures 3 and 4 show the extracted centerline velocity plot of both algorithms. It can be clearly seen, that the interrogation window produces a smoothing at the nozzle which results in a decay of the estimated velocity. EMQD on the other hand nicely reproduces the trend up to the orifice. The same averaging effect is responsible for the lower maximal velocity ($\approx 80\%$) for MQD compared to EMQD ($\approx 90\%$). The missing spatial averaging for EMQD is the reason for the rugged profile. However, the normalized velocity profiles match nicely for both methods.

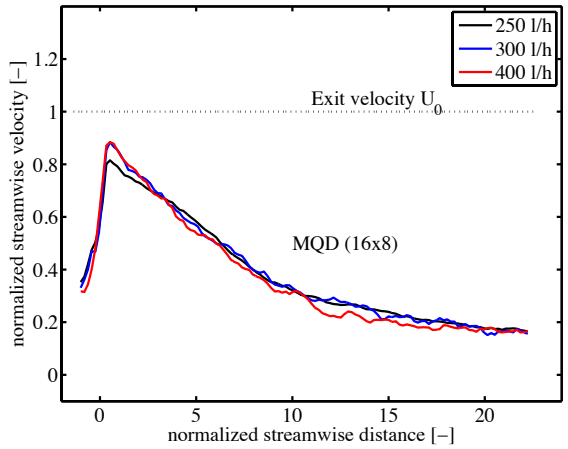

Fig. 3. Centerline profiles of the streamline velocity estimated by MQD for 16×8 pixel interrogation window

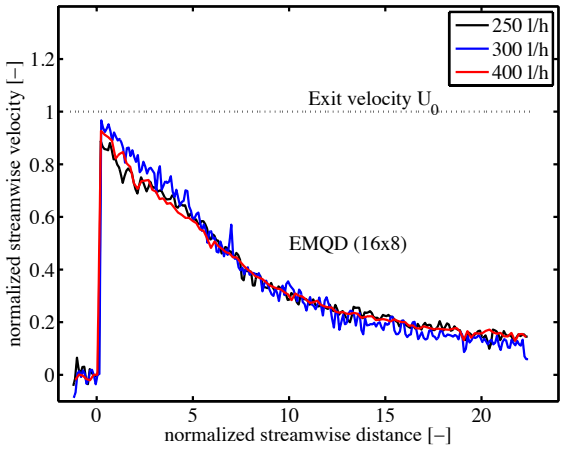

Fig. 4. Centerline profiles of the streamline velocity estimated by EMQD for 16×8 pixel interrogation window

4.2 Cross correlation and Cross correlation averaging

The jet images were processed by a state-of-the-art PIV software in order to estimate the average velocity field. Standard iterative multigrid with implicit image deformation was applied to yield a final interrogation window size of 32×16. In this case the standard evaluation method is not capable of properly estimating the outflow velocity ($\approx 60 - 70\%$). The reason is a combination of spatial averaging and temporal averaging which is not robust. Similar to figure 3 PIV exhibits the effect of a decaying velocity towards the nozzle which also caused by the finite sized interrogation window. Results for *C*ross correlation averaging (CCA) are not shown as it yielded very unreliable results with strong pixel-locking artifacts. The reasons that are still being investigated especially on the background that this technique yielded acceptable data for the oil plume sequence in section 5.

4.3 Pixel matching

This method is actually a variant of single pixel ensemble correlation (Westerweel et al, 2004) and should yield similar results to the cross correlation techniques (see figure 6). This algorithm can be easily parallelized as it acts on every pixel individually without influence by the neighboring pixels. This disadvantage is that the result is rather noisy but the trend is clearly visible. Subsequent spatial smoothing (similar to the interrogation window) improves the result at the cost of reduced spatial resolution (figure 7). The maximal estimated velocity is around 90% and due to the single-pixel method there is no velocity decay towards the nozzle.

4.4 Time matching

If the pixels on the centerline are plotted against their temporal development (x-axis), all moving structures generate specific patterns according to their velocity (see figure 8). The faster a structure is, the steeper is the orientation of the patterns in this plot. Moving away from the nozzle, the slope of these patterns decreases. The slope is directly related to the velocity of the structures moving in the image. In order to determine the slope, we tested for different δx starting from neighboring pixel rows to two rows with 29 rows in between. The two rows were cross correlated in order to determine the best time lag. The data was upsampled by a factor of 10 to enforce a smooth maximum and a successful Gaussian fit of the peak. For small $\delta x \leq 5$ the maximum is too close to the border to allow accurate fitting. Therefore, we selected $\delta x = 15$ to estimate the velocity. Since the velocity profile is smooth the velocity estimate with such a large δx does not significantly affect the result in the far-field. However, in the near-field the choice of δx is too small because the displacement $d_{\max}$ is of the same order and the Gaussian fit is not working properly. Therefore, at the nozzle exit the velocity is overestimated by 10% to 20%, depending on the exit velocity of the experiment.

4.5 Optical Flow

The most well-known *optical flow* method of Horn and Schunck (1981) was applied to determine instantaneous velocity field for the first 5000 images of each measurement. The number of images was reduced because convergence was already achieved but also to spare time and disk space. The balancing parameter α has to be chosen in such a way that it renders the mathematical task uniquely solvable but does not change the problem itself by much. We found $\alpha = 0.0002$ an optimal choice and the averaged velocity profiles are shown in figure 10. It can be clearly be seen that the exit velocity is not reached at all. The maximal velocity at best reaches 60% of the reference velocity U_0. The effect of spatial regularization can be seen in the smoothly bent velocity profile close to the nozzle. The

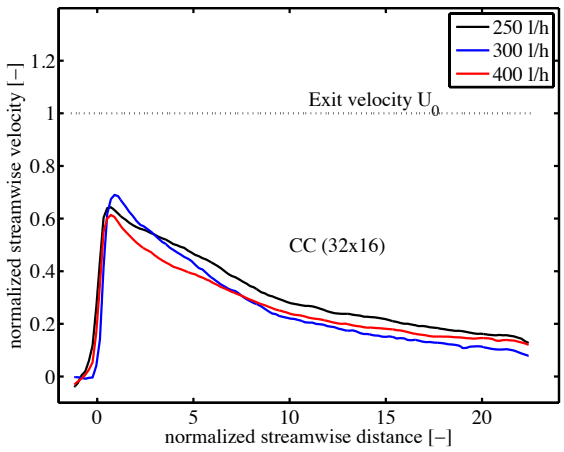

Fig. 5. Centerline profiles of the streamline velocity estimated by CC

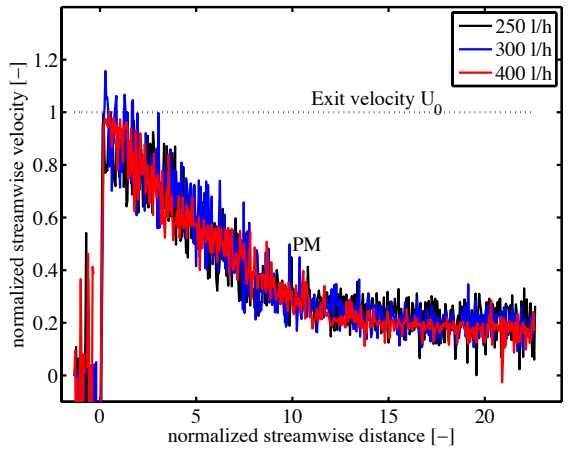

Fig. 6. Centerline profiles of the streamline velocity estimated by PM

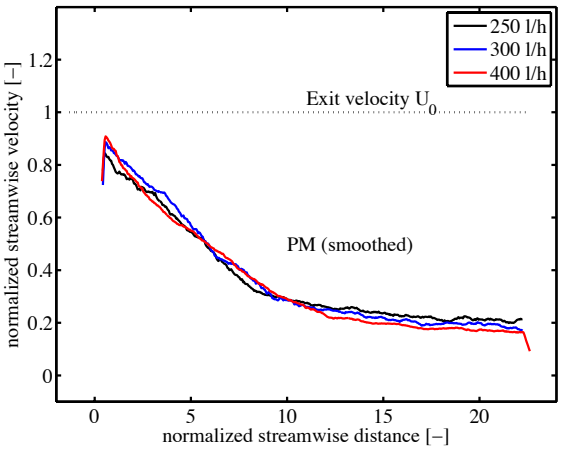

Fig. 7. Centerline profiles of the streamline velocity estimated by PM smooth by a boxcar function with 16×8 pixel support

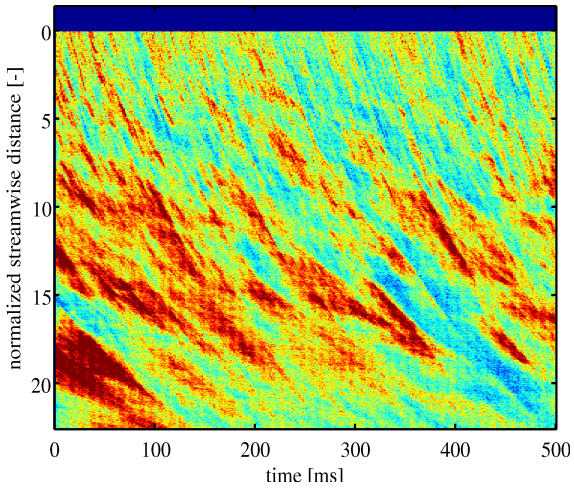

Fig. 8. Space-time plot of all pixels on the centerline axis of the jet

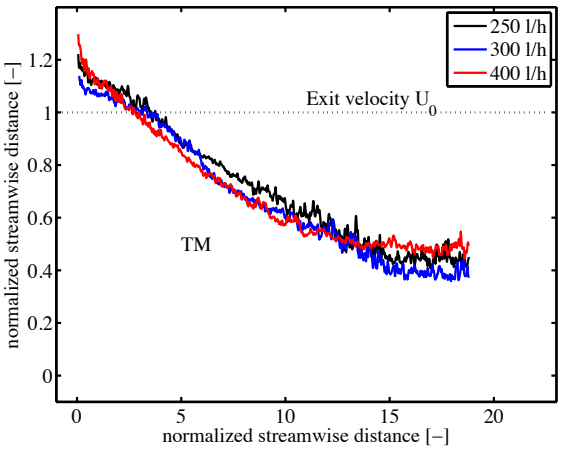

Fig. 9. Centerline profiles of the streamline velocity estimated by TM with $\delta x = 15\,\mathrm{px}$

algorithm uses a smooth profile to connect zero velocity of the stationary nozzle with the maximal velocity in the near-field of the jet.

The calculated instantaneous velocity fields were used to produce a velocity field of the maximal velocities that appear in the entire sequence (Maximal Optical Flow, MOF). The top lines in figure 10 show the MOF results which are close to the expected theoretical velocity profile of a turbulent jet. A constant potential core velocity ($x = 0..5D$) is followed by decaying profile (in theory $\propto {}^{1}/_{x}$). The potential core velocity fits the exit velocity of the jet with a slight overshoot.

4.6 Ensemble Optical Flow

Rather than averaging instantaneous velocity fields, this method makes use of the entire images sequence in order to find an optimal velocity field that suits consecutive image pairs best. The algorithm can produce estimates for $\alpha = 0$ because of the temporal averaging. It is related to the Time-Matching (TM) algorithm because it is based on the temporal aspect of intensity changes at every pixel. Consequently, the results look similar to TM in figure 9. There is an overestimation of up to 20% close to the nozzle. Measurement 2 is apparently different to the others because of the extremely noisy pro-

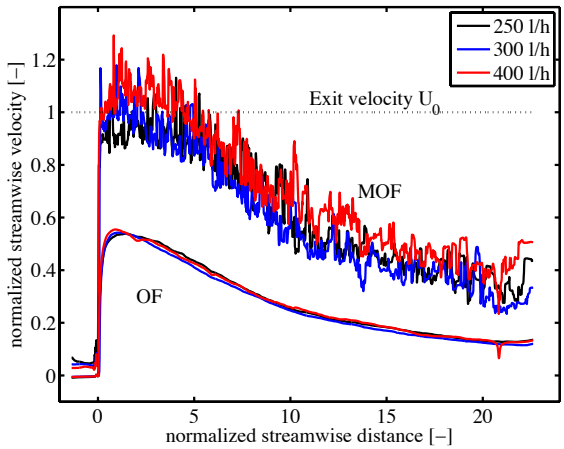

Fig. 10. Centerline profiles of the streamline velocity estimated by OF and MOF with $\alpha = 0.0002$

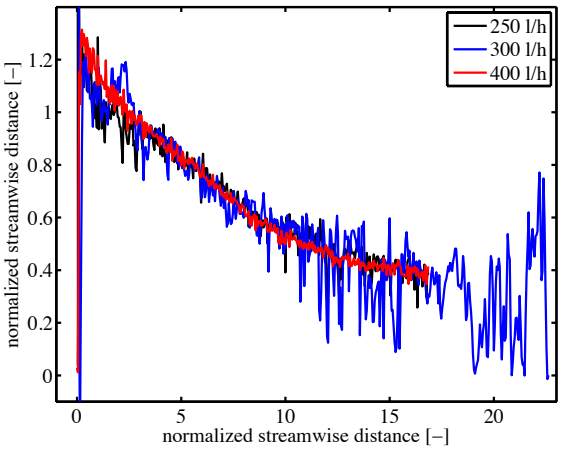

Fig. 11. Centerline profiles of the streamline velocity estimated by EOF with $\alpha = 0$

file. EOF has problems in reproducing the velocity in the far-field because of the poor signal to noise ratio. The variations due to noise are of the same order as the gradients of the image structures. Here, spatial averaging could overcome this deficiency but was not applied yet. The accuracy of this technique is highly dependent on the correlation length of the image structures. According to Staack and Garbe (2011) one can determine the error by knowing the correlation length. Besides, the algorithm is extremely fast because it treats all pixels individually and computes just statistical moments.

5. Results of oil plume analysis

5.1 Image stabilization

Prior to motion estimation processing image stabilization was necessary because the ROV was continuously swaying due to the strong currents at the bottom of the ocean. For this purpose we used SIFT (Lowe, 1999), an scale and translation-invariant algorithm that detects feature points in two images and aligns them using image transformation. In particular we have chosen the corners of the nozzle as feature points which allowed to stabilize the position and the scaling of 2 min of streaming video (3000 frames). The effect can clearly be seen in figure 12, where the left image is the average image without correction and the right image with SIFT correction. The fact that the image sequences were acquired by a consumer grade camera in the POV and were made available as a compressed image stream led to difficulties that the algorithms have to deal with. The images contain also motion blur because of the long exposure time and the frame rate is also quite low, so that turbulent motion changes the intensity structures rapidly.

5.2 Centerline velocity U_c

The presented algorithms were applied to estimate the streamwise velocity at the centerline of the oil plume sequence. Figure 14 shows the results of all algorithms and figure 13 the velocity along the center of the visible jet. Velocities of around 15 pixels per frame could be observed by simple (visual) examination of the images but due to the complex upstream conditions the issuing flow is fully turbulent with both high speed and low speed structures. Apparently the algorithms perform very different for such difficult images. The exit velocity ranges from 4 $\mathrm{px/_{frame}}$ to 10 $\mathrm{px/_{frame}}$ depending on the algorithm. However, there are some similarities in the pattern of the motion estimate. In many cases there is high velocity estimated in the center and on both edges of the jet (14(a), 14(b), 14(f) and 14(g)) but for other algorithms this feature is not observable. Assuming MOF performs equally well on these images as in the turbulent jet, we can determine the maximal velocity that appears at each pixel (figure 14(i)). The velocity is quite constant at about 25 px/frame at the center of the jet.

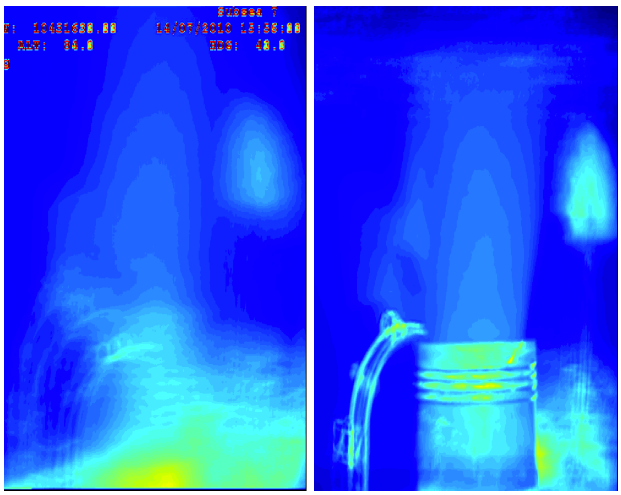

Fig. 12. Shown on the left is the uncorrected averaged image of the entire sequence and on the right the SIFT corrected average image.

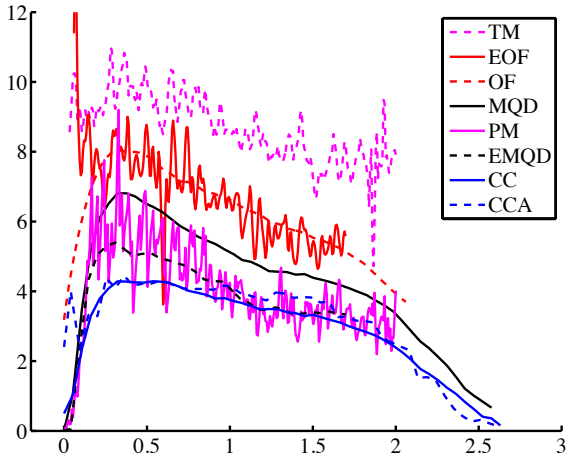

Fig. 13. Centerline velocity U_c of the oilspill jet determined by the presented algorithms

6. Discussion

The presented material shows that the estimation of velocity from opaque images is a challenging task. Depending on the algorithm the results differ by up to a factor of 2 for the oil plume image sequence. The general trend and shape of the velocity profile is comparable for all of the investigated methods but the magnitude varies significantly. On the other hand the results of the laboratory experiment are in better agreement with each other. In general, ensemble averaging methods perform better than standard averaging methods which was already observed for particle images (Meinhart et al, 2000). With respect to the laboratory experiment, the differences within these two groups are small. As a conclusion we can state that in the context of non-standard fluid dynamics images, the result very much depends on the choice of evaluation method. Any results and from such images have to be interpreted with caution. It has to be kept in mind that all of the described techniques attempt to capture the spatial and temporal motion of distinct structures within the image. For the turbulent jet experiment this included the movement of the structures on the boundary as well as on the interior of the jet. In contrast the oil/gas plume sequences mainly visualize the exterior motion of the oil/water interface and occlude the interior of the jet. With assumptions on the jet profile it nonetheless is possible to estimate the volume flow rate from the interface motion.

References

Astarita T (2007) Analysis of weighting windows for image deformation methods in PIV. Experiments in Fluids 43:859–872

Barron J, Fleet DJ, Beauchemin SS (1994) Performance of optical flow techniques. International Journal of Computer Vision 12(1):3–77

Beauchemin SS, Barron J (1995) The computation of optical flow. ACM Computing Surveys 27(3):433–467

Bosbach J, Kühn M, Wagner C (2009) Large scale particle image velocimetry with helium filled soap bubbles. Experiments in Fluids 46(3):539–547

Corpetti T, Courty N (2007) Crowd motion capture. Computer Animation and Virtual Worlds

Corpetti T, Mémin E, Pérez P (2002) Dense Estimation of Fluid Flows. IEEE Transactions on pattern analysis and machine intelligence 24(3):365–380

Corpetti T, Heitz D, Arroyo G, Mémin E, Santa-Cruz A (2005) Fluid experimental flow estimation based on an optical-flow scheme. Experiments in Fluids 40(1):80–97

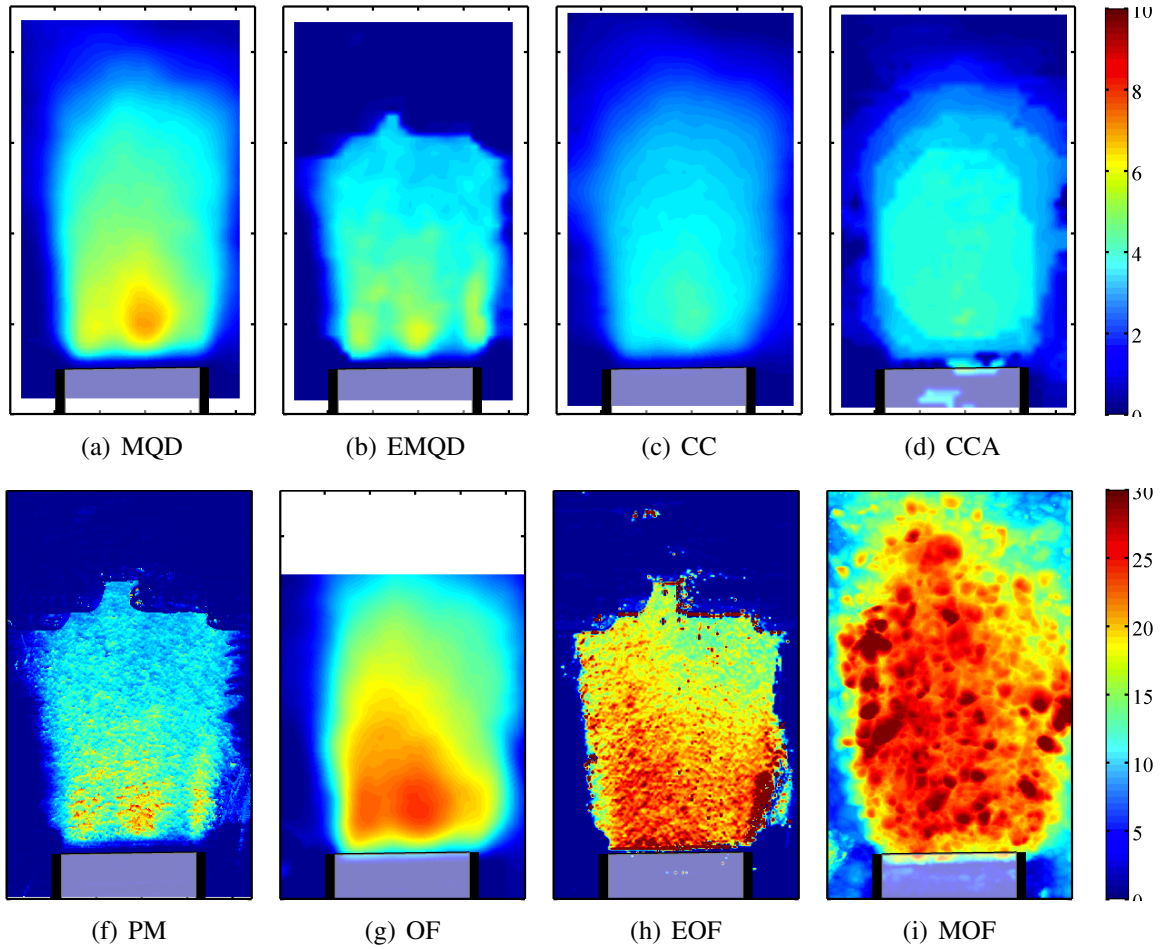

(a) MQD (b) EMQD (c) CC (d) CCA

(f) PM (g) OF (h) EOF (i) MOF

Fig. 14. Streamwise velocity determined by the presented algorithms. The top color coding in pixels per frame belongs to the figures 14(a)–14(h) and the other to the figure 14(h)

Crone TJ (2010) Magnitude of the 2010 Gulf of Mexico Oil Leak. Science 330(6004):634

Crone TJ, McDuff RE, Wilcock W (2008) Optical plume velocimetry: a new flow measurement technique for use in seafloor hydrothermal systems. Experiments in Fluids 45(5):899–915

Delnoij E, Westerweel J, Deen N, Kuipers J, Van Swaaij W (1999) Ensemble correlation PIV applied to bubble plumes rising in a bubble column. Chemical Engineering Science 54:5159–5171

Flow Rate Technical Group (2010) Deepwater Horizon Release Estimate of Rate by PIV. Tech. rep., United States Department of the Interior, URL `http://www.doi.gov/deepwaterhorizon/loader.cfm?csModule=security/getfile&PageID=68011`

Garbe C, Roetmann K, Beushausen V, Jähne B (2008) An optical flow MTV based technique for measuring microfluidic flow in the presence of diffusion and Taylor dispersion. Experiments in Fluids 44(3):439–450

Gui L, Merzkirch W (1996) A method of tracking ensembles of particle images. Experiments in Fluids 21(6):465–468

Horn BKP, Schunck B (1981) Determining Optical Flow. Artificial Intelligence 17:185–203

Lowe D (1999) Object recognition from local scale-invariant features. Computer Vision, 1999 The Proceedings of the Seventh IEEE International Conference on 2:1150–1157 vol. 2

Lucas B, Kanade T (1981) An iterative technique of image registration and its application to stereo. In: Proc. 7th Int'l Joint Conf. on Artificial Intelligence, pp 674–679

McKenna S, McGillis W (2002) Performance of digital image velocimetry processing techniques.

Experiments in Fluids 32(1):106–115

McNutt M, Camilli R, Guthrie G, Hsieh P, Labson V, Lehr B, Maclay D, Ratzel A, Sogge M (2011) Assessment of Flow Rate Estimates for the Deepwater Horizon / Macondo Well Oil Spill. Flow Rate Technical Group report to the National Incident Command, Interagency Solutions Group. Tech. rep., United States Department of the Interior, URL http://www.doi.gov/deepwaterhorizon/loader.cfm?csModule=security/getfile&PageID=237763

Meinhart CD, Wereley ST, Santiago J (2000) A PIV algorithm for estimating time-averaged velocity fields. Journal of Fluids Engineering 122:285–289

Okamoto K, Nishio S, Saga T, Kobayashi T (2000) Standard images for particle-image velocimetry. Measurement Science and Technology 11:685–691

Quénot GM, Pakleza J, Kowalevski T (1998) Particle image velocimetry with optical flow. Experiments in Fluids 25:177–189

Raffel M, Willert CE, Wereley ST, Kompenhans J (2007) Particle image velocimetry: a practical guide, 2nd edn. Springer, Berlin

Ronneberger O, Raffel M, Kompenhans J (1998) Advanced evaluation algorithms for standard and dual plane particle image velocimetry. 9th International Symposium on Applications of Laser Techniques to Fluid Mechanics

Savaş O (2011) A Visual Study of the Near Field of Turbulent Jets and Implications for Estimating Accidental Discharges. Tech. rep., University of California Berkeley

Staack K, Garbe CS (2011) Ensemble Optical Flow. In: Flucome 2011, Keelung, Taiwan, pp 1–9

Westerweel J, Geelhoed P, Lindken R (2004) Single-pixel resolution ensemble correlation for micro-PIV applications. Experiments in Fluids 37(3):375–384

Willert CE, Gharib M (1991) Digital particle image velocimetry. Experiments in Fluids 10:181–193